Materials and Design 190 (2020) 108569

Contents lists available at ScienceDirect

Materials and Design

journal homepage: www.elsevier.com/locate/matdes

The influence of fiber orientation and geometry-induced strain concentration on the fatigue life of short carbon fibers reinforced polyamide-6

Luca Quagliato [a], Yonghee Kim [a], João Henrique Fonseca [a], Dosuck Han [a], Seungjong Yun [b], Hyungtak Lee [c], Nara Park [d], Hyungyil Lee [a], Naksoo Kim [a,*]

[a] Department of Mechanical Engineering, Sogang University, Seoul, South Korea
[b] Research and Development Center, Donghee Industrial Company, Ulsan, South Korea
[c] Polymer R&D Team, GS Caltex R&D Center, Daejeon, South Korea
[d] Korean Institute of Carbon Convergence Technology, Jeonju, South Korea

HIGHLIGHTS

- The shell-core structure, with different fiber orientation and length distributions, influences the mechanical properties
- The strain redistribution on the polymer matrix is different for static failure, low cycles fatigue and high cycles fatigue
- Fiber length and orientation distributions are mapped onto the structural simulation to account for the material properties
- The local strain concentration and stress triaxiality were utilized to estimate the stress state on the part
- The utilized mapping procedure allows has high accuracy in predicting the fatigue life of complex shape components

GRAPHICAL ABSTRACT

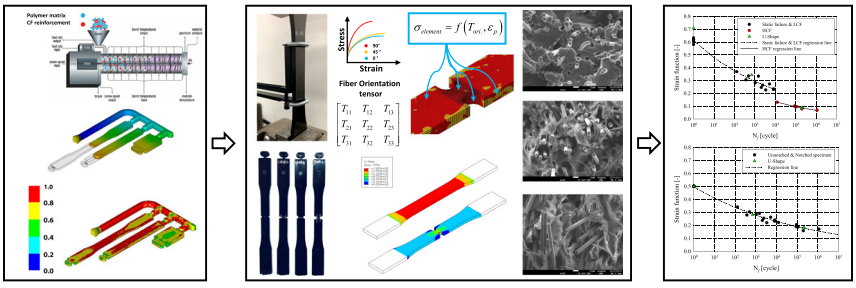

ARTICLE INFO

Article history:
Received 23 December 2019
Received in revised form 13 February 2020
Accepted 13 February 2020
Available online 14 February 2020

Keywords:
Thermoplastic polymer
Injection molding process
Strain approach
Stress and strain concentration
Stress triaxiality
Fatigue life estimation

ABSTRACT

Static and fatigue mechanical properties of a polyamide-6 reinforced with a 20% weight fraction of short carbon fibers (PA6-20CF) material were investigated by means of static and fatigue tensile tests on both unnotched and notched specimens. SEM pictures were also taken on the fracture surface of specimens tested under static, low cycle failure (LCF) and high cycle failure (HCF) conditions, allowing to correlate the cycles to failure with the deformation pattern of the polymer matrix. Accordingly, two strain-approach-based fatigue models were developed and allowed accounting for the different influence of stress, and strain, concentration on the fracture behavior for static failure, LCF and HCF. To account for the variation of mechanical properties with fiber orientation, Autodesk Moldflow Insight simulations were performed, and the resulting fiber orientations were mapped into Abaqus via the mapping program Autodesk Helius. The model was validated by utilizing it for the prediction of the fatigue life of a complex shape part, showing a maximum error equal to 13.7%, in comparison to experimental results.

* Corresponding author at: Adam Schall Hall #601, Sogang University, 35, Baekbeom-ro, 04107 Seoul, South Korea.
E-mail address: nskim@sogang.ac.kr (N. Kim).

https://doi.org/10.1016/j.matdes.2020.108569

1. Introduction

Fiber filler thermoplastic polymers, and the injection molding process, are largely utilized in several industrial compartments thanks to their lightweight, low cost and high productivity [1–3]. However, both static and fatigue mechanical properties of components made of fiber-reinforced thermoplastic polymers are strongly influenced by the fiber orientation, as a result of the polymer flow during the injection molding process. Hence, the complex fiber orientation distribution (FOD) caused by the injection molding process has been investigated by many scholars in order to define its influence on the mechanical properties of short glass fibers (SGF) reinforced polyamide [4–7] and short carbon fiber (SCF) reinforced polyamide [8,9]. Moreover, also the fiber length distribution ought to be properly accounted for due to their influence on the effectiveness of the fibers in reinforcing the base polymer [10–12].

In injection molded specimens, the mechanical properties along the injection flow direction present higher failure stress and a lower failure strain, in comparison to the direction orthogonal to the injection one [13]. This effect increases with the fiber volume fraction [14–16] and it is influenced by the thickness of the specimen. Moreover, in injection molded parts, the fiber orientation along the thickness of the specimen is not constant but it develops in a sort of shell-core structure where, in the shell, the fibers are strongly aligned along the polymer flow direction whereas, in the core, are transversally aligned [4,17,18]. From the analytical and numerical point of view, the utilization of a anisotropic rotary diffusion model [19,20] combined with a fiber length degradation model based on buckling force and hydrodynamic loading of the fiber [20,21] allow a precise estimation of the fiber orientation and length distributions according to the geometry of the considered component. Hence, both models have been adopted in the injection molding process simulation presented in this paper.

As concerns fatigue life models for reinforced thermoplastic polymers, different interpretations for this phenomenon have been proposed in the literature considering the influence of fiber length, fiber content and FOD as well as variable amplitude loading and multiaxial stress effect [22]. Most of the literature works focus on the influence of the fiber orientation on the mechanical properties and fatigue life by mean of strain-based approaches [4,5,15,24] and stress-based approaches [6,7,23]. Regardless of strain- or stress-based approach, most of the literature contributions seem to deal with SGF reinforced polymers and only a few papers account for the static mechanical properties of SCF polymers [9]. In addition to that, the stress concentration theory [25] seems to be applied for the estimation of the fatigue life in case of geometrical irregularities [26,27] but, for the case of complex shape, the estimation of the fatigue stress concentration factor might be complicated and lead to estimation errors. In fact, for the case of simple-geometry specimens, the fatigue life can be easily estimated on the basis of the notch geometry [28,29] but, for more complex shapes the application of the stress concentration theory is not straightforward because a combination of rounded and sharp edges may be present in the area surrounding the fracture onset.

Although several literature contributions dealt with the definition of models for the estimation of the fatigue life of polymers, no contribution seems to approach it from the perspective of utilizing either the stress triaxiality or the strain concentration as criteria for the evaluation of the fatigue life of injection molded parts. In addition to that, due to the large utilization of SGF reinforced materials in the industry, in comparison to SCF ones, only a few literature contributions seem to deal with the mechanical properties characterization of SCF reinforced polymers.

Thus, the aim of this paper is to provide a solid material characterization background for the PA6-20CF material and, based on the results of the SEM image analysis, interpret the different material behavior at LCF, including the static failure, and HCF, highlighting the lower, or higher, capability of the PA6 base polymer of deforming, thus of absorbing damage, before the final failure. In addition to that, attention has been also focused on the debonding and pull-out mechanisms between fiber and thermoplastic matrix, and the results of this analysis are reported in the paper as well. Based on these results of the material properties characterization and image investigation, the two fatigue life prediction model are proposed and are based on the concept that the strain, or stress, concentration, arising in case of local geometries irregularities, have a decreasing effect from static failure to LCF and finally to HCF.

To investigate the static and fatigue mechanical properties of the PA6-20%CF material, ASTM-D 638-02a-TYPE I specimens have been injection molded in a specimen shot, where bending and impact tests specimens (not utilized in the research presented in this paper) are also present. In order to investigate the effect of local strain concentration, notched specimens have been machined from the unnotched ones (injection-molded ASTM-D 638-02a-TYPE I) in order not to alter the original fiber orientation and have been tested under static and cyclic loading conditions. In addition to that, to account for the different material properties resulting from different FOD along 0° (injection direction), 45° and 90° direction, plates have been injection-molded and ASTM-D 638-02a-TYPE IV specimens have been machined on their centers.

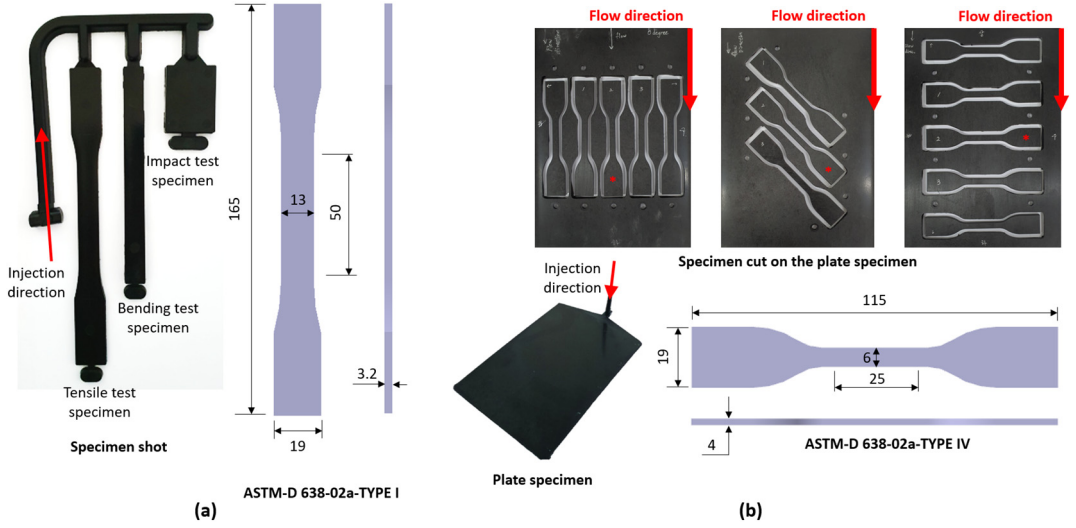

Fig. 1. (a) Specimen shot, with the runner, and ASTM-D 638-02a-TYPE I tensile specimen dimensions. (b) Plate specimen, with the runner, 0°,45° and 90° directions-cut specimens and ASTM-D 638-02a-TYPE IV tensile specimen dimensions.

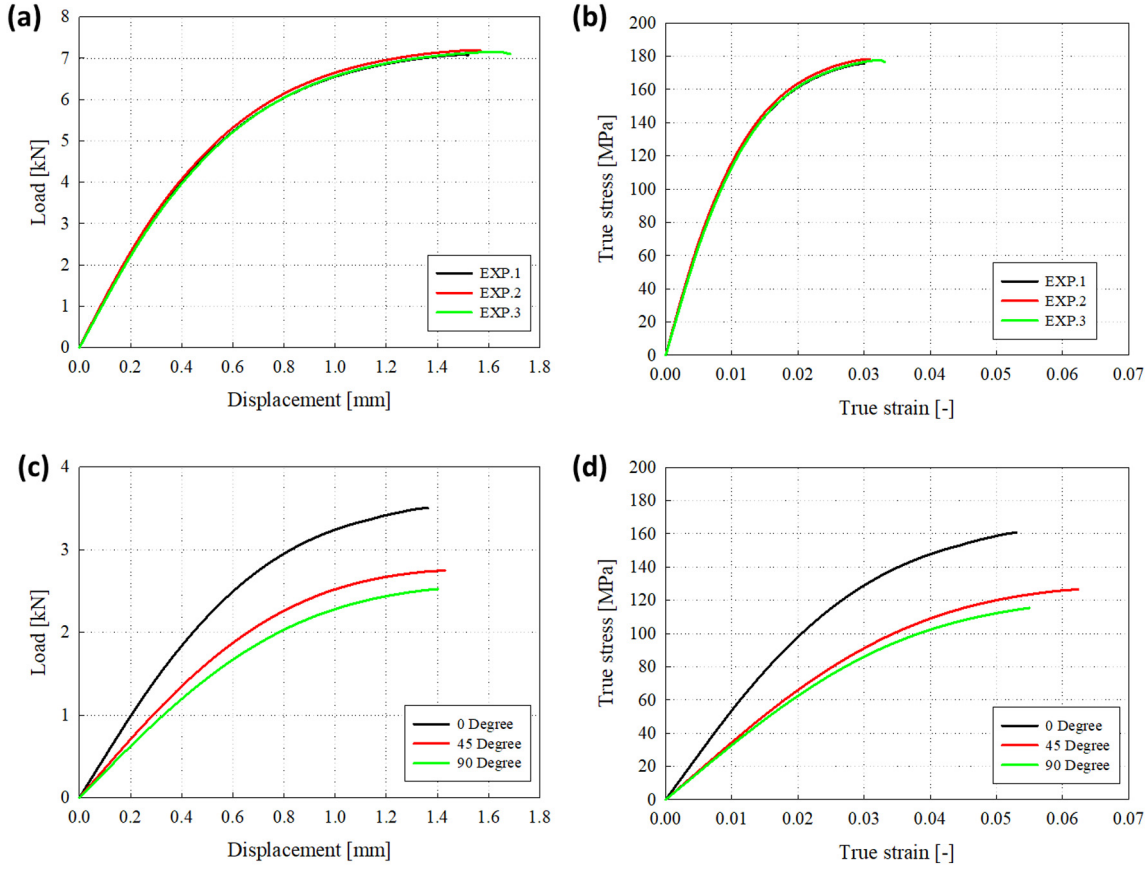

Fig. 2. Static mechanical properties of the PA6-20%CF material for the ASTM-D 638-02a-TYPE I (a, b) and ASTM-D 638-02a-TYPE IV (c, d) specimens.

From the numerical point of view, the fiber orientation in the specimens has been accounted for by means of finite volume simulations implemented in the commercial software Moldflow Insight and the results have been mapped into the relevant ABAQUS/Standard finite element simulation models by means of the Autodesk Helius program. The combined utilization of process and structural simulations allows a precise estimation of the effect of the local fiber orientation and length distributions on the mechanical properties of the material, also for complex geometries and real industrial components [30]. The proposed mapping procedure and fatigue models have been utilized for the estimation of the fatigue life of a complex injection-molded U-shape geometry showing that the proposed approach allows predicting the cycles to failure with a reasonable error, equal to 13.7%.

2. Specimen characteristics

The pellets utilized for the manufacturing of the tensile and bending specimens employed for the mechanical properties characterization of the PA6-20CF material have been manufactured utilizing a mix of Kolon Plastic KN111 polyamide-6 (PA6) [31] and the Torayca T700S short carbon fibers [32]. By means of the injection molding process, two different parts have been injection molded and the relevant images and specimen dimensions are reported in Fig. 1a, for the specimen shot, and in Fig. 1b, for the plate specimen, respectively. From the specimen shot (Fig. 1a), only the tensile specimen has been utilized in the research presented in this paper.

On the other hand, from the plates, tensile test specimens have been cut along 0° (injection flow direction), 45° and 90° directions according

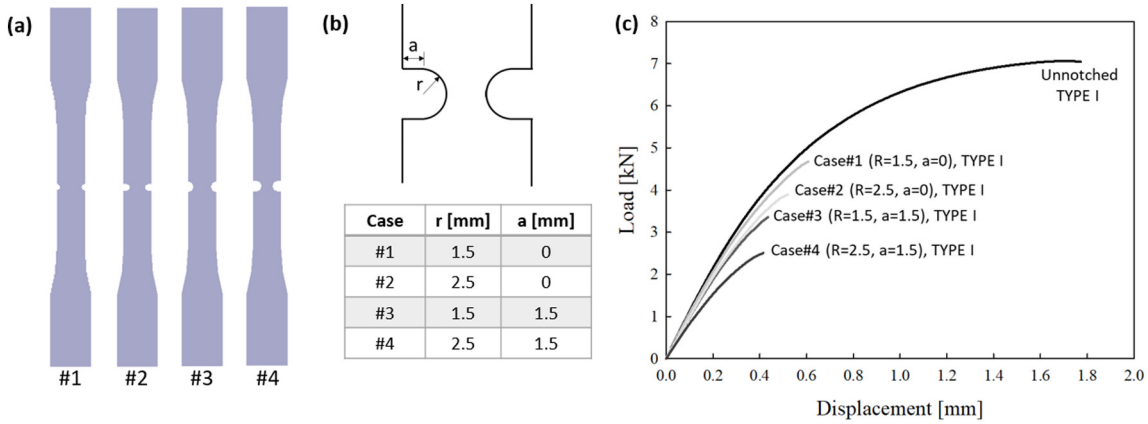

Case	r [mm]	a [mm]
#1	1.5	0
#2	2.5	0
#3	1.5	1.5
#4	2.5	1.5

Fig. 3. (a) Notched specimens cut from the tensile ones, (b) notch dimensions and locations and (c) load-stroke curves of the unnotched and notched specimens.

to the ASTM-D 638-02a-TYPE IV specification and the specimen marked with "*" (central one) have been utilized, as shown in Fig. 1b. The direction-dependent material properties obtained from the ASTM-D 638-02a-TYPE IV (Fig. 1b) have been utilized as input for the numerical simulation model whereas the tensile specimen on the specimen shot (Fig. 1a), have been utilized for both static and fatigue tests and for the manufacturing of the notched specimen.

3. Characterization of the static mechanical properties

The static mechanical properties of the PA6-20CF material have been characterized by means of tensile tests carried out at the speed of 2 mm/min, under room temperature conditions of 20 °C, and by utilizing the Instron 3367 testing machine. Before the experiments, the specimens have been dried for 6 h at 120 °C by means of the HanKook System Co. Ltd. HKOD-50 oven dryer where a heat flow of 12 m^3/h has been utilized in order to remove the humidity absorbed after the injection molding process and before the test. After the drying operation, the weight of the specimens have been checked, prior to the tensile tests, in order to assure the proper removal of the humidity, finding the specimen weight in the range 10.3 g ± 0.1 g, measured with a precision balance with a resolution of ±0.1 g.

During the tensile test, the stroke has been measured by means of Instron 2630 extensometer with a calibrated gauge length of 50 mm, for the ASTM-D 638-02a-TYPE I specimen, and 25 mm, for the ASTM-D 638-02a-TYPE IV specimen. The load-stroke and true stress-strain curves for both specimen geometries reported in Fig. 2. The slight difference in the mechanical properties of the 0° (polymer flow direction) between the TYPE I and TYPE IV specimens is explained by the different fiber orientation distribution throughout the specimens' thicknesses, as it will be shown in Section 8 of the paper. This difference is properly accounted for in the injection molding numerical simulation as well as during the mapping procedure, as detailed in Section 7 of the paper.

As previously mentioned, in order to investigate the influence of a complex stress-states on the static and fatigue failures, notched specimens have been manufactured by performing CNC operations on the injection-molded ones (specimen shot, ASTM-D 638-02a-TYPE I), considering different notch geometries, as shown in Fig. 3a. The dimensions of the notches manufactured on the specimens have been measured after the CNC operation and all have been found in a range of ± 0.05 mm in comparison to the theoretical ones, reported in Fig. 3b. Due to the presence of the notches, neither the engineering stress-strain nor the true stress-strain curves can be precisely calculated directly from the experimental load-stroke curves alone, due to the stress concentrations on the tip and on the notch. Hence, in this section of the paper, only the load-stroke curves resulting from the experiments are reported in Fig. 3c (case#1 to case#4). For the sake of comparison, in Fig. 3c, the unnotched specimen curve EXP.2 (Fig. 2a), is reported and, as expected, the higher the depth of the notch the lower the stiffness as well as the failure stroke.

Table 1
Results of the fatigue experiments on unnotched specimens (experimental results).

Case	Mean stroke [mm]	Stroke amplitude [mm]	σ_{vM_max} [MPa]	R [−]	ε_{max} [−]	ε_{min} [−]	ε_a [−]	N_f
#1U	0.5	0.3	142.8	0.40	0.018	0.005	0.007	8217
#2U	0.6	0.3	149.1	0.52	0.020	0.006	0.007	8140
#3U	0.6	0.4	156.1	0.36	0.023	0.005	0.009	1049
#4U	0.7	0.25	152.1	0.70	0.022	0.010	0.006	112,497
#5U	0.7	0.2	149.1	0.76	0.020	0.011	0.005	198,936
#6U	0.7	0.3	156.1	0.64	0.023	0.009	0.007	3386
#7U	0.8	0.35	163.4	0.66	0.027	0.010	0.009	2066
#8U	0.6	0.25	146.1	0.60	0.019	0.007	0.006	92,286
#9U	0.5	0.2	135.4	0.58	0.015	0.007	0.004	1,127,661

Table 2
Fatigue experiment conditions for the notched specimens.

Case	Geometry	Mean stroke [mm]	Stroke amplitude [mm]	N_f
#1N	#1	0.30	0.10	5214
#2N	#1	0.36	0.11	367
#3N	#2	0.30	0.10	2400
#4N	#2	0.30	0.15	130
#5N	#3	0.28	0.07	490
#6N	#3	0.26	0.04	12,630
#7N	#4	0.23	0.13	1500
#8N	#4	0.25	0.05	91,220

4. Characterization of the fatigue properties

In this section of the paper, the results of the fatigue experiments carried out on both unnotched and notched tensile specimens (ASTM-D 638-02a-TYPE I), are reported. In order to characterize the fatigue behavior of the PA6-20%CF material, an $\varepsilon - N_f$ approach has been utilized thus, as reported in Table 1, each experiment is characterized by a mean stroke and stroke amplitude. For sake of a clear understanding, the fatigue experiments of the unnotched specimens, Table 1, are named with their relevant case number followed by the letter "U" and have been designed, taking as reference the load-stroke curve of the unnotched specimen EXP.2 (Fig. 2a), in order to obtain a spectrum of cycles to failure ranging from approximately 10^3 to over 10^6 cycles. During the experiments, the stroke has been measured by means of Instron 2620 extensometer with a 50 mm gauge length. The results, in terms of strain amplitude, maximum stresses and cycles to failure are reported in Table 1 where the parameter ε_a is defined as half of the strain amplitude as $(\varepsilon_{max} - \varepsilon_{min})/2$. As concerns the fatigue experiments on notched specimens, the notches dimensions reported in Fig. 3b have been utilized and the experimental conditions, as well as the cycles to failure (N_f), are reported in Table 2. For the notched specimens the letter "N", preceded the case number, has been utilized to differentiate them from the unnotched specimens.

5. SEM microscopic image analysis

In order to understand the different effects of static failure, LCF and HCF on the PA6-20%CF material, scanning electron microscope (SEM) images have been taken on the fracture surface of specimens after the final failure. For the investigation, the JSM-7100F/JEOL FE-SEM machine with a resolution equation to 3.0 nm (at 15 kV) and a Pt coating have been applied to the specimen surfaces before the test. The proposed images are all relevant for the unnotched specimen but similar conclusions can be drawn also for the notched specimen.

Firstly, the locations for the images have been selected by considering the results of the injection molding simulations on the tensile specimen of the specimen shot (Fig. 1a). Although the injection molding

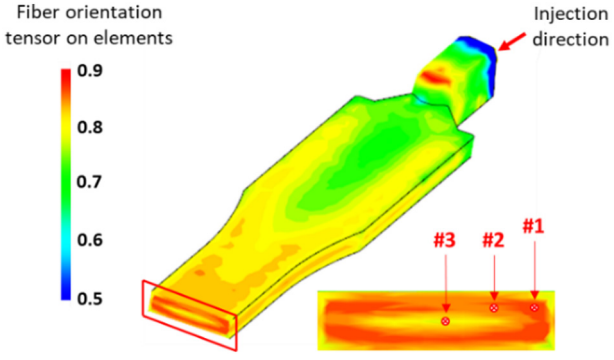

Fig. 4. Fiber orientation tensor on elements for the unnotched tensile specimen (ASTM-D 638-02a-TYPE I) in the middle cross-section.

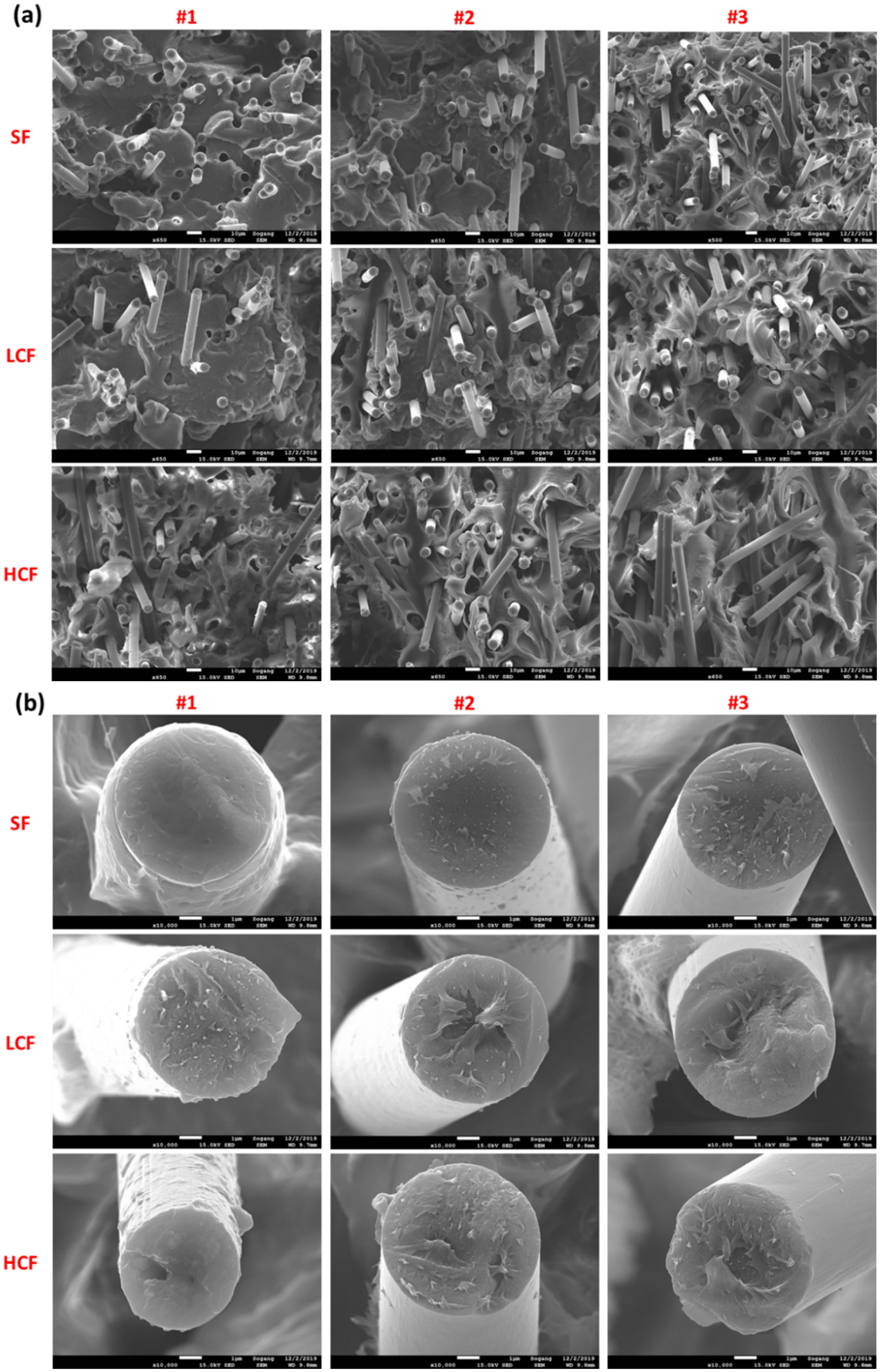

Fig. 5. (a) Matrix failure surface and (b) detail of the fiber top surface location #1, #2 and #2 in case of static failure (SF), low cycles fatigue (LCF) and high cycles fatigue (HCF).

process simulation is detailed in Section 7 of the paper, for sake of explaining the reasoning behind the choice of the location for the SEM picture analysis, the results of the fiber orientation tensor on the mesh elements for the tensile specimen of the specimen shot (ASTM-D 638-02a-TYPE I) is reported in Fig. 4.

According to the fiber orientation tensor results reported in Fig. 4, three different locations for the SEM analysis have been chosen and are identified as #1, #2 and #3. The #1 location is placed at the center shell region of the specimen, where the fiber orientation is highest, thus where a significant amount of fibers are aligned with the injection flow direction. The point #2 is located in the transition zone between the shell and the core of the specimen whereas the #3 at the center of the specimen, where the amount of fibers aligned with the plastic flow direction is the lowest, for the considered section. The SEM images have been taken in these three locations and are relevant for: i) static failure (EXP.2, Fig. 2a), ii) LCF (CASE #2U) and iii) HCF (CASE #5U). Detailed pictures of the polymer matrix failure surfaces are reported in Fig. 5a. In addition to that, in Fig. 5b, the surface of a single fiber for the three above-mentioned locations and loading conditions are reported as well. In Fig. 5, SF, LCF and HCF stand for static failure, low cycle failure and high cycle failure, respectively. For the case of the static failure, the clean fracture surface and the clean holes left by the pullout of the fiber clearly show the absence of matrix deformation before the fracture for point #1 and #2 whereas point #3 shows a more irregular surface, standing for a higher deformation of the base polymer before the final fracture.

These irregularities of the fracture surface of the base polymer increase with increasing number of cycles with an increasing effect from point #1 to point #3. This fact is correlated to the higher capability of the polymer matrix to redistribute the strain, thus to deform more, for HCF rather than static failure or LCF, which also results in a high deformation, in the matrix, after the failure.

In addition to that, according to the results presented in Fig. 5a, the lower the fiber orientation tensor, the lower the fiber alignment along the plastic flow direction (same as loading direction), the higher the capability of the matrix of deforming during the load application. For high fiber orientation tensor values, a large percentage of the load is carried by the fibers whereas, for low fiber orientation tensor values, more load is applied to the matrix, a fact which increases its deformation. The phenomenon increases for HCF, resulting in an increased deformation of the matrix starting from the top left picture to the bottom right one.

Another interesting aspect is related to the analysis of the fiber top surface, as reported in Fig. 5b. For the static failure, the top surface of the fiber presents an increasing polymer matrix residual from point #1 to point #3 and this effect becomes increasingly evident from SF to LCF to HCF. For the case of LCF point #3, a clear shear fracture surface is visible on the top of the fiber but, due to the mixing operation operated by a twin-screw in the pellet extrusion process and in a single screw in the injection molding process, it is not possible to define whether this failure has been caused by the manufacturing process or by the experiment. According to the differences of the fracture surface, a clear variation from absence, or low, deformation to diffuse and large deformation of the polymer matrix is identified and is aimed to be accounted for by the two fatigue life estimation models presented in the following section of the paper.

6. Fatigue model formulations

As previously mentioned, two different fatigue life models are proposed in this paper and their details are described in this section of the paper. Both models have been developed considering an $\varepsilon - N_f$ approach utilizing, as a starting point, the Manson-Coffin model, Eq. (1).

$$\frac{(\varepsilon_{p,\,\max} - \varepsilon_{p,\,\min})}{2} = \Delta\varepsilon_p = A(N_f)^c \tag{1}$$

In the original Manson-Coffin model, only the plastic strain contribution is considered whereas, in the proposed models, the total strain is accounted for. In order to directly compare the proposed models with that of Eq. (1), the model constants have been defined as A and c and, for the original Manson-Coffin model, represents the true strain at fracture ε_f' and the slope of the fatigue life curve c. The first of the two proposed models is shown in Eq. (2) and, as previously mentioned, static failure and LCF are accounted for by Eq. (2.1) whereas HCF by Eq. (2.2).

$$\left(\frac{\varepsilon_{\max,i} - \varepsilon_{\min,i}}{2\varepsilon_{f,i}}\right)^{(1-m_1)} \left(\frac{\sigma_H}{\overline{\sigma}_{vM}}\right)^{m_1} = A_1(N_f)^{c_1} \quad (2.1)$$

$$\left(\frac{\varepsilon_{\max,i} - \varepsilon_{\min,i}}{2\varepsilon_{f,i}}\right)^{(1-m_2)} \left(\frac{\sigma_H}{\overline{\sigma}_{vM}}\right)^{m_2} = A_2(N_f)^{c_2} \quad (2.2) \tag{2}$$

The reasoning behind the choice of separating these two contributions resides in the analysis of the SEM analysis of the fracture surface of the matrix polymer, as presented in the previous section of the paper, as well as in the interpretation of the results of the fatigue experiments. For static failure and LCF, the polymer matrix has a low capability of redistributing strains, and stresses, during the loading application, a fact which results in less deformation of the polymer matrix of the specimen. This fact is clear in the clean fracture surface 5a. On the other and, for HCF, the matrix is highly deformed, a fact that suggests the progressive strain of the polymer before the fracture.

In order to account for these two different phenomena, two equations, with the threshold between LCF and HCF set at 10^4 cycles, have been developed. In Eq. (2), the first term represents the ratio between the strain amplitude and the static failure strain for a considered geometry and allows accounting for the mean strain correction. In this paper, the mean strain is utilized as a sort of stress ratio (R) correction and allows accounting for the mean stroke effect on fatigue life N_f.

On the other hand, the second term represents the ratio between the hydrostatic stress and the von Mises equivalent stress and is defined as the stress triaxiality. The stress triaxiality is utilized to account for the influence of the geometry on the fatigue life and, for instance, for the case of a notched specimen, the stress triaxiality is highest at the tip of

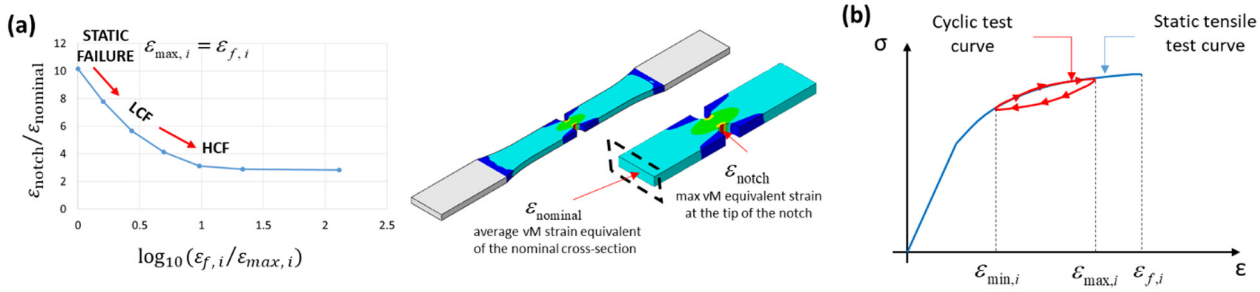

Fig. 6. (a) Progressive reduction of the strain concentration at the tip of the notch for increasing N_f and (b) schematic cycling loading test for the explanation of the terms of Eq.(3).

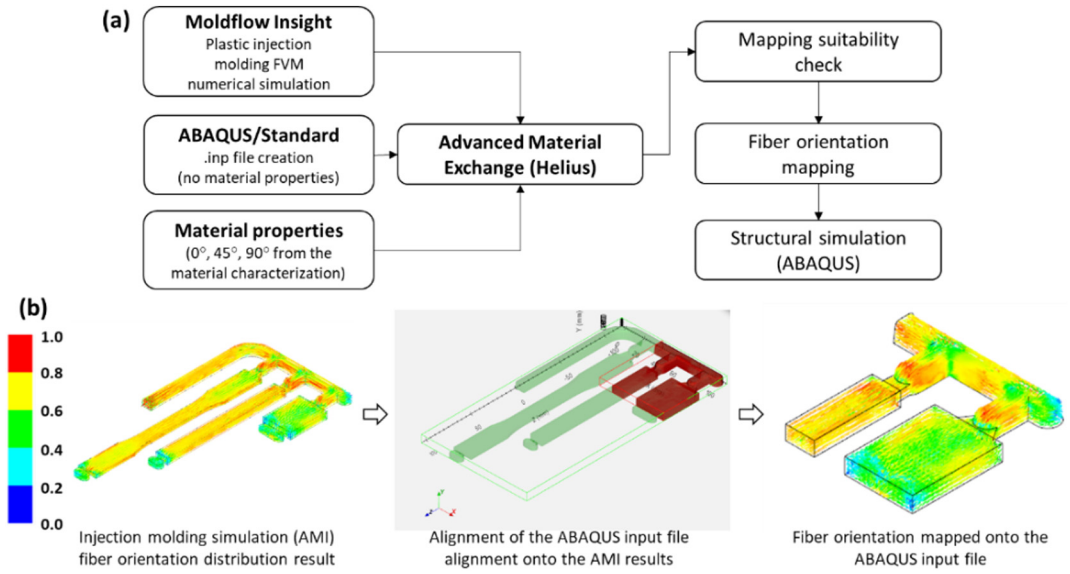

Fig. 7. (a) Numerical simulations implementation procedure and (b) mapping operation flow in the Advanced Material Exchange Helius module.

the notch which also corresponds the onset point for the fracture. The two exponents m_1 and m_2 allows calibrating the relative influence of the stress triaxiality, with respect to the mean-strain-corrected strain amplitude, for LCF and HCF separately. As it will be shown in the Results section, separately accounting for LCF and HCF allows obtaining a good correlation between the regression line and experimental data as well as to reasonably predict the fatigue life of the U-Shape validation part. As concerns the second proposed model, presented in Eq. (3), its formulation is more compact thanks to the inclusion of the third term, which allows accounting for the progressive reduction of the influence of the strain concentration for an increasing number of cycles to failure, as shown in Fig. 6a.

$$\left(\frac{\varepsilon_{\max,i}-\varepsilon_{\min,i}}{2\varepsilon_{f,i}}\right)\left(\frac{\varepsilon_{f,S\_UN}}{\varepsilon_{f,i}}\right)\left[1+\log_{10}\left(\varepsilon_{f,i}/\varepsilon_{\max,i}\right)\right]^{-1}=A_3\left(N_f\right)^{c_3} \quad (3)$$

The effect of the argument of the logarithmic function, defined as the ratio between the static failure strain for the unnotched specimen and the maximum strain for a considered case, is to account for the progressive capability of the polymer matrix of deforming for HCF, rather than LCF or static failure. To better explain the role of the various parameters shown in Eq. (3), they have been all summarized in the schematic diagram reported in Fig. 6b whereas $\varepsilon_{f,\,S\_UN}$ represents the static failure strain of the unnotched specimen, namely (EXP.2, Fig. 2a). Finally, the effect of the second term of Eq. (3) is to allow to compute a single value for the model constant A for all the static failure for both unnotched and notched specimens, thus increasing the accuracy of the regression function.

If the static failure of the considered component ($\varepsilon_{f,\,i}$) is not known, as for the case of an on-going design, this value can be estimated from the results of a numerical simulation by means of an anisotropic failure criterion. In this case, the failure strain is estimated, from the results of the numerical simulation, as the total equivalent von Mises strain of the mesh element which reaches first the critical damage.

The model constants for the two proposed models have been determined on the basis of the experimental and numerical results in terms of stress and strain fields arising on both unnotched and notched and have been subsequently applied for the estimation of the fatigue life of a U-Shape part. The results concerning the two proposed models are reported in the Results section of the paper.

7. Numerical model implementation

Numerical simulation models have been implemented in order to investigate the effect of the fiber orientation on the mechanical properties, as well as to define the stress-strain evolution for the notched specimen and the validation (U-Shape) part. In this research, three different commercial software have been utilized, namely: i) Autodesk Moldflow Insight/Synergy 2019 (AMI) for the plastic injection molding process; ii) Advanced Material Exchange Helius 2019 (AME) for the mapping operation and iii) ABAQUS 2017 for the structural simulation, Fig. 7.

In the first phase, the plastic injection molding simulation has been implemented in AMI considering the thermo-mechanical material properties of the base polymer and fiber [31,32], also available in the AMI material library.

The model has been meshed with tetrahedral elements of 1 mm side length for a total count of 1.12×10^6 elements. The simulation has been set, as in the specimen production process, considering a molten material temperature (at the nozzle) of 285 °C, a mold temperature of 85 °C, and a cooling time of 25 s. The whole injection system is modeled with cold runners. In order to account for the fiber orientation and fiber length distributions, as a consequence of the shot specimen geometry and injection molding process, the anisotropic rotary diffusion model [19] combined with the fiber length degradation model [21] have been employed.

In the second phase, the result of the injection molding simulation has been inputted in the AME program [33] along with the mechanical properties obtained from the material characterization of the ASTM-D 638-02a-TYPE IV specimens (Fig. 1d). In order to account for the

Table 3
Model constants and definitions for the Ramberg-Osgood flow stress model and for the modified Hill'48 yield function.

Parameter	Definition	Value
K	Strength coefficient	80.6 MPa
n	Hardening exponent	10.16
E_m	Polymer matrix elastic modulus	4.25 GPa
E_f	Fibers elastic modulus	105.6 GPa
α_m	Weight factor for the fiber direction	2.125
β_m	Weight factor for the direction normal to the fibers	1.214
$\lambda_{m,\,I}$	First eigenvalue of the fiber orientation matrix in the region with strong fiber alignment with the polymer flow	0.85

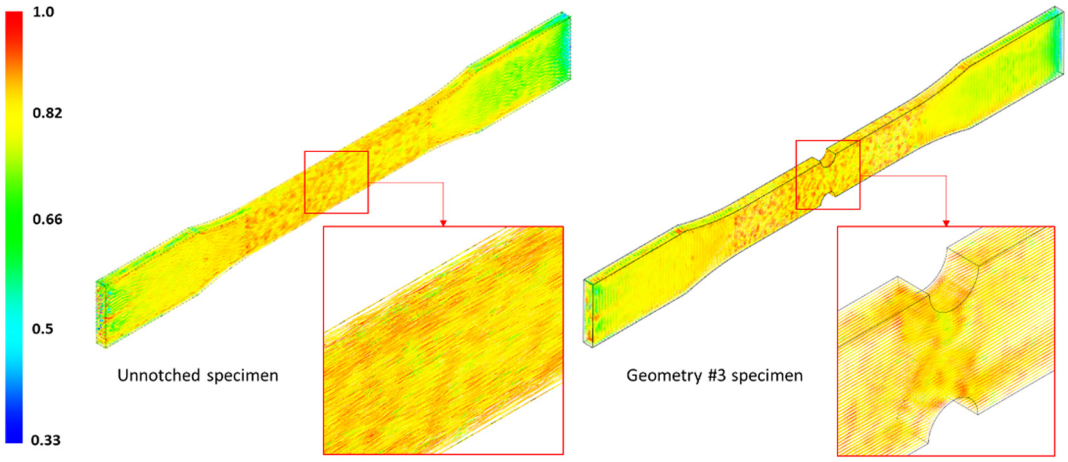

Fig. 8. Mapping operation of the fiber orientation of the unnotched specimen on the geometry #3 notched specimen.

variation of the mechanical properties according to fiber orientation distribution developing in the part, the Ramberg-Osgood flow stress model, Eq. (4), has been utilized in combination with a modified Hill'48 yield function, Eq. (5), where the α and β parameters act as scaling factors to the yield function. α accounts for the fiber direction whereas $\beta$for the two directions transversal to the fibers, making Eq. (5) to be an orthotropic yield function.

$$\sigma = E^{1/n}(K)^{(n-1)/n}\left(\varepsilon_{p,eff}\right)^{1/n} \tag{4}$$

$$\sigma_{eff} = \sqrt{\frac{(\alpha\sigma_{11}-\beta\sigma_{22})^2 + (\beta\sigma_{22}-\beta\sigma_{33})^2 + (\beta\sigma_{33}-\alpha\sigma_{11})^2 + 6\left[(\sigma_{12})^2 + (\sigma_{23})^2 + (\sigma_{31})^2\right]}{2}} \tag{5}$$

The α and β parameters are calculated for each element of the mesh on the basis of the local FOD, taking as reference the values on the region of the model where the first eigenvalue of the fiber orientation tensor is maximum, as shown in Eq. (6). In Eq. (6), λ_I defines the first eigenvalue of the fiber orientation tensor of the considered element. The reference values, defined as α_m, β_m and $\lambda_{m,\,I}$, are calculated in the AME module and, along with the Ramberg-Osgood model constants for the PA6-20CF material, are reported in Table 3.

$$\alpha(\lambda_I) = \theta + \left[\frac{(\alpha_m-\theta)}{(\lambda_{m,I}-1/2)}\right](\lambda_I-1/2) \quad , \quad \beta(\lambda_I) = \theta + \left[\frac{(\beta_m-\theta)}{(\lambda_{m,I}-1/2)}\right](\lambda_I-1/2) \tag{6}$$

At this stage, the mechanical properties have been calculated for each element of the mesh on the basis of its fiber orientation tensor, taking as reference the global coordinate system of the injection molding simulation. The same element-based fiber orientation-dependent mechanical properties shall be mapped onto the ABAQUS input file mesh. The mapping operation is carried out aligning the tensile specimen (ABAQUS inp. file model) on the same location of the same specimen in the specimen shot (AMI) as shown in Fig. 7b, for the case of the U-Shape part.

This procedure is of high importance for the case of the notched specimen where the portion of material removed by the CNC operation can be accounted for without altering the original fiber orientation and length distributions originated during the injection molding process. This is clearly visible from the result mapping shown in Fig. 8, where the fiber orientation of the unnotched specimen is mapped into geometry #3 (Table 2).

The Abaqus numerical model for the ASTM-D 638-02a-TYPE I specimen has been modeled considering the C3D10 element, for a total count of 17,438 elements, and by setting as rigid the two jig regions (gray part of the model in Fig. 9a). Also the U-Shape part has been meshed with the same element type for a total count of 30,480 elements and has been set by considering as rigid only the portions of the part where the tensile jigs have actually left indentation signs (Fig. 9b).

Due to the concavity of the impact specimen surface, the jigs are not able to close on the whole surface, as highlighted in Fig. 9b, as also accounted for in the numerical simulation.

8. Results

By means of the injection molding numerical simulation implemented in AMI, the fiber orientation in the tensile specimen of the specimen shot (Fig. 1a) and the plate specimen (Fig. 1b) have been

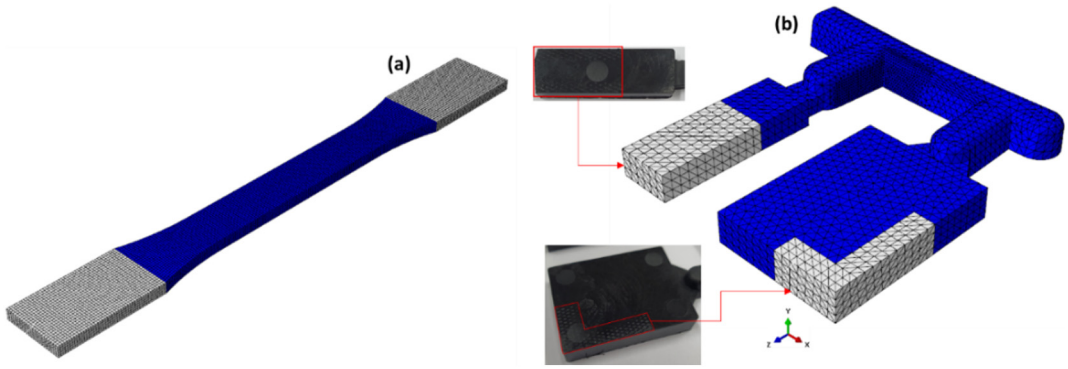

Fig. 9. (a) Numerical model implementation for the ASTM-D 638-02a-TYPE I specimen, (b) for the U-Shape specimen considering the tensile jigs indentation signs on the specimen surface.

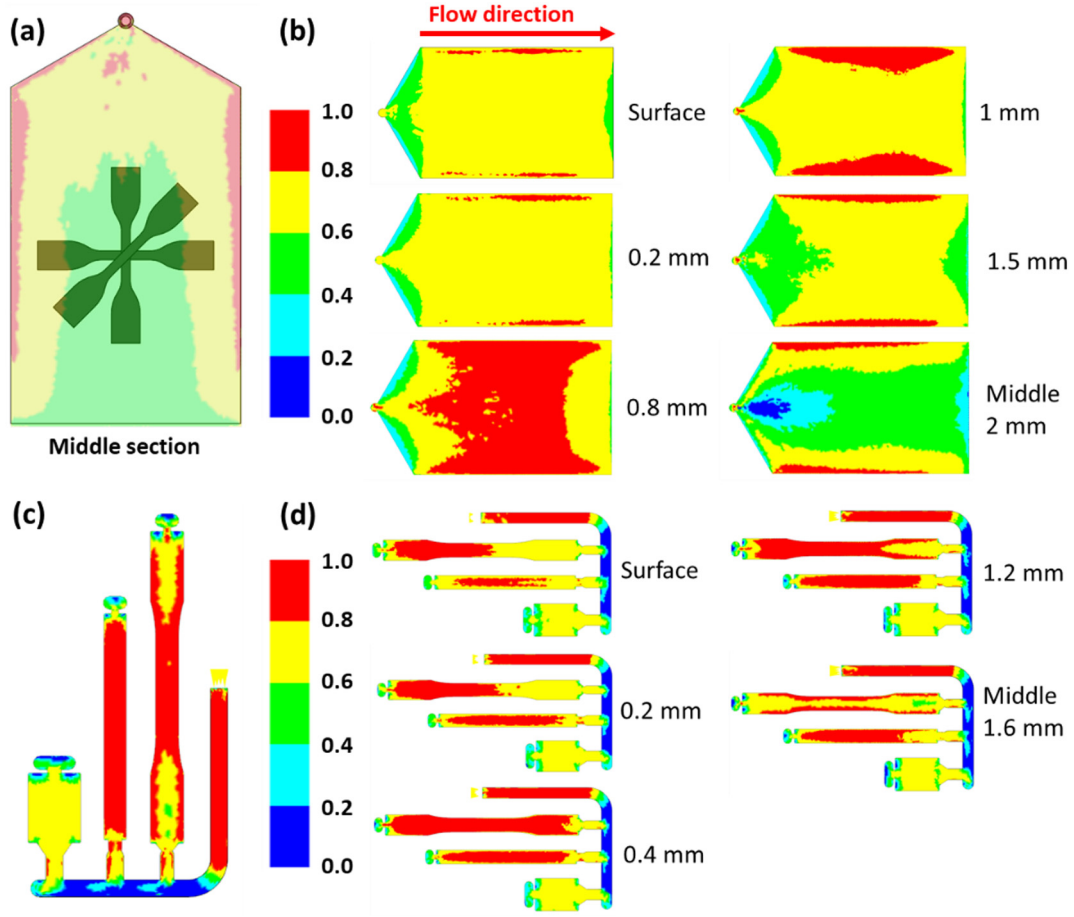

Fig. 10. Fiber orientation distribution (overall) and throughout the thickness for plate specimen, (a) and (b), and for the tensile specimen (specimen shot), (c) and (d).

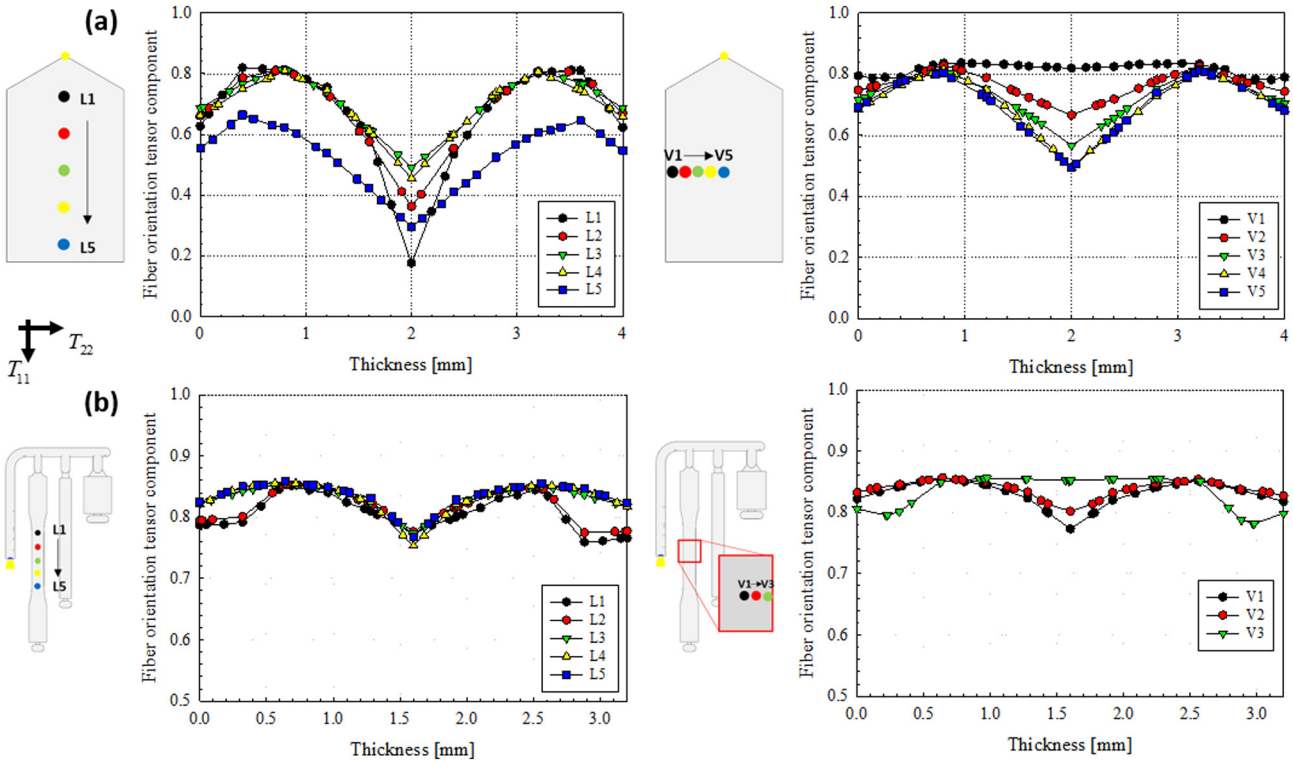

Fig. 11. Fiber orientation tensor T_{11} component variation throughout the thickness and for different longitudinal and transversal positions (a) for the plate specimen and (b) for the tensile specimen on the specimen shot.

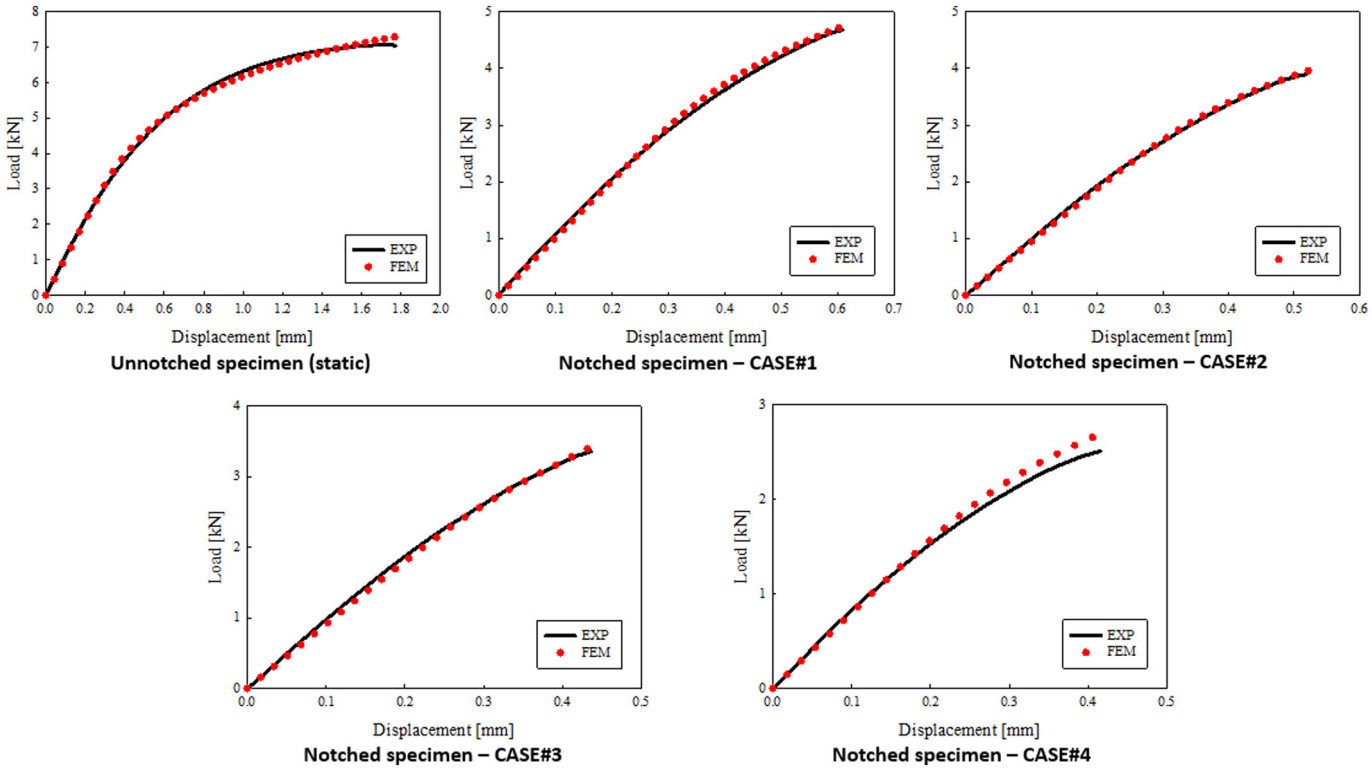

Fig. 12. Experimental and numerical results for the load-stroke curve of tensile specimens (static experiments).

investigated. The cutting location for the ASTM-D 638-02a-TYPE IV tensile specimens on the plate specimen, along 0° (injection direction), 45° and 90°, Fig. 10a, have been chosen considering that the fiber orientation in the center location, Fig. 10b, is the most similar one with that of the tensile specimen, of the tensile shot (Fig. 10d). As concerns the tensile specimen, from the specimen shot, (Fig. 10c) its fiber orientation in the 0.4 mm plane is almost completely aligned with the injection flow direction but, as for the case of the plate specimen (Fig. 10b), it is not constant throughout the thickness, Fig. 10d. The shell-core structure of the fiber orientation, presented in Fig. 10, is typical of the injection molding process, as also highlighted in the previous research results [4,17,18]. This variation of the fiber orientation along the cross-section of the specimen results in a variation of the local mechanical properties, properly accounted by means of the mapping procedure reported in the previous chapter of the paper. The results presented in Fig. 10 are organized starting from the surface of the specimen to its central axis (middle) considering the results to be symmetric and have been plotted considering, as a reference, the material flow direction. The variation of the fiber orientation, throughout the thicknesses of the parts, for the plate specimen and the tensile specimen are reported in Fig. 11a and b, respectively and have been interpreted as the reason for the slight difference in the mechanical properties previously shown in Fig. 2b (TYPE I specimen) and Fig. 2d (TYPE IV specimen). By means of the numerical simulation frame presented in the previous section of the paper, a single set of mechanical properties for the PA6-20%CF material has been calculated, as presented in Table 3. Accordingly, structural numerical simulations for both unnotched and notched specimens have been implemented utilizing the mapping procedure detailed in Fig. 7 and allows accounting for the notch geometry influence, as shown in Fig. 8. The accuracy of the inverse calibration of the mechanical properties is shown in Fig. 12, where the experimental and numerical load-stroke curves for the static experiment of unnotched and notched specimens are reported. In addition to that, the results of stress and strain amplitudes for the notched experiments, for both static and fatigue experiments, calculated by means of the implemented numerical simulation procedure, are summarized in Table 4.

The progressive reduction of the mean load, for increasing number of cycles, for four different cases, two unnotched (#3U and #5U) and two notched (#3N and #8N) specimens, are shown in Fig. 13. Similar results have been obtained for the other cases and, for this reason, are not included in the manuscript.

As concerns the U-Shape part, utilized for the validation of the proposed fatigue models for the case of complex geometries, it is has been manufactured by cutting it from the specimen shot and has been subjected to both static and cyclic tensile test, as shown in Fig. 14a.

The fiber orientation distribution, mapped onto the ABAQUS input file by the procedure detailed in chapter 7, is reported in previous

Table 4
Results of the static and fatigue experiments on notched specimens (from FEM).

Static tensile test results

Geometry	Failure stroke [mm]	σ_{vM_max} [MPa]	ε_{max} [−]	N_f
#1	0.61	231.7	0.104	1
#2	0.52	213.4	0.093	1
#3	0.45	220.8	0.074	1
#4	0.42	236.6	0.099	1

Fatigue tests results

Case	Mean stroke [mm]	Stroke amplitude [mm]	σ_{vM_max} [MPa]	R [−]	ε_{max} [−]	ε_{min} [−]	ε_a [−]	N_f
#1N	0.30	0.10	193.7	0.67	0.046	0.013	0.016	5214
#2N	0.36	0.11	220.6	0.67	0.060	0.019	0.021	367
#3N	0.30	0.10	187.1	0.65	0.038	0.011	0.014	2400
#4N	0.30	0.15	204.9	0.59	0.068	0.015	0.026	130
#5N	0.28	0.07	194.4	0.64	0.046	0.012	0.017	490
#6N	0.26	0.04	176.3	0.71	0.031	0.012	0.010	12,630
#7N	0.23	0.13	213.5	0.45	0.061	0.018	0.022	1500
#8N	0.25	0.05	194.4	0.77	0.038	0.018	0.01	91,220

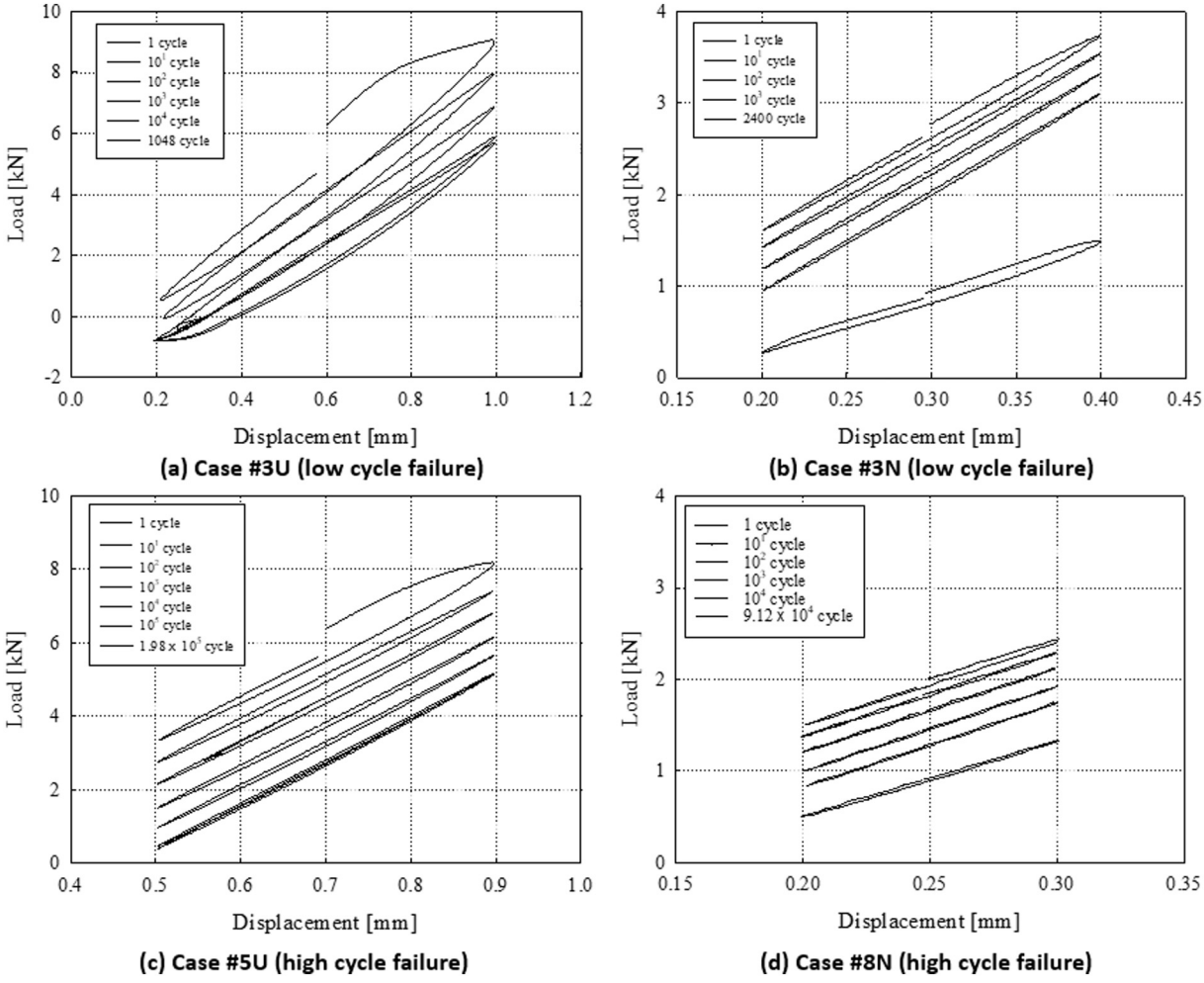

Fig. 13. Load vs displacement curves for (a) #3U, (b) #3N, (c) #5U and #8N.

Fig. 7b whereas the stress distribution in the crack onset region and the comparison between experimental and numerical load-stroke curves are reported in Fig. 14b and c, respectively. The investigation of the stress and strain field on the fracture onset section of the U-Shape part allowed identifying the node at which these values are maximum, subsequently utilized for the extraction of the data to be inputted in the two proposed fatigue life models. Same concerning the U-Shape part, three static tests, and three fatigue experiments have been carried out.

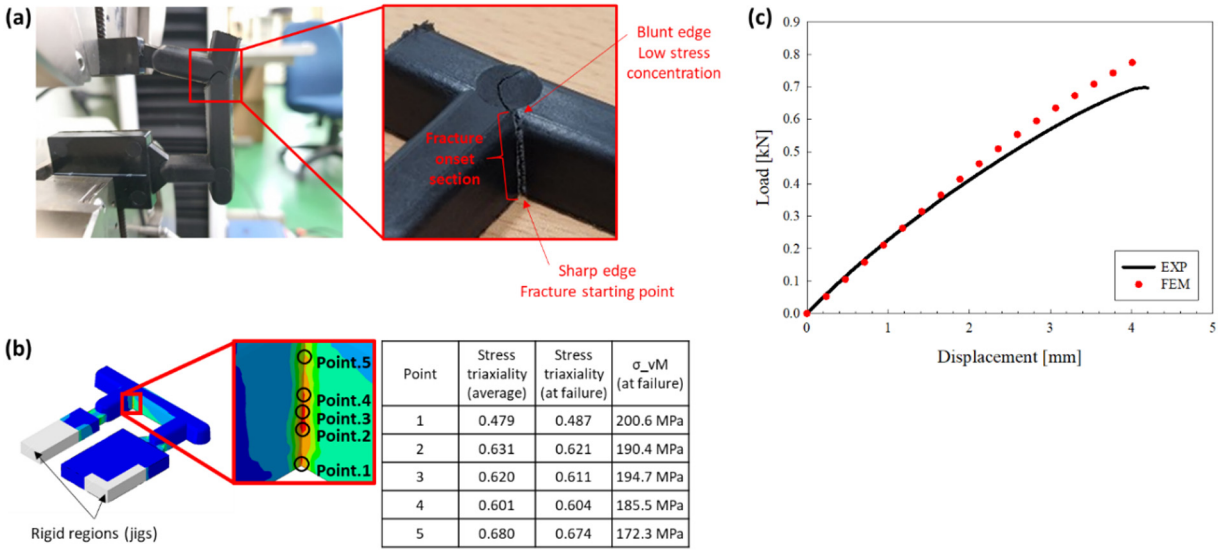

Point	Stress triaxiality (average)	Stress triaxiality (at failure)	σ_vM (at failure)
1	0.479	0.487	200.6 MPa
2	0.631	0.621	190.4 MPa
3	0.620	0.611	194.7 MPa
4	0.601	0.604	185.5 MPa
5	0.680	0.674	172.3 MPa

Fig. 14. (a) On-going experiment and fracture section for the U-Shape part, (b) numerical stress distribution on the fracture section of the U-Shape part and (c) comparison between numerical and experimental load-stroke curves for the U-Shape part.

Table 5
Constant for the fatigue life estimation models.

Model	Equation validity range	Constant	Value
Eq. (2.1)	$1 \le N_f \le 10^4$	m_1	0.523
		A_1	0.611
		c_1	−0.107
Eq. (2.2)	$N_f > 10^4$	m_2	0
		A_2	0.542
		c_2	−0.151
Eq. (3)	$N_f \ge 1$	A_3	0.496
		c_3	−0.084

In order verify the repeatability of the experiments also for the case of the validation part, two experiments have been carried out with the same mean stroke and stroke amplitude (2.5 mm, 0.5 mm) whereas the third one with a higher mean stroke and stroke amplitude (2.85 mm, 0.85 mm). The target is to achieve an LCF and an HCF, in order to properly validate the two proposed fatigue models on all the three failure conditions covered by the models.

Considering altogether the results presented in Figs. 12 and 14c, the maximum and average errors between experimental and numerical results, calculated as the ratio between the area integrals of the load-stroke curves, are equal to 7.3% and 2.6%, showing the reliability of the adopted procedure for the inverse calibration of the material properties of short fibers reinforced polymer manufactured by means of injection molding process.

9. Discussion

Based on the experimental and numerical results on unnotched and notched specimens, as presented in the previous sections of the paper, the RMS regression method has been applied separately to models of Eqs. (2.1) and (2.2) for the two sets of constants, one for the $1 \le N_f \le 10^4$ range and one for the $N_f > 10^4$ range, respectively. The correlation factor (R^2) for the first set is equal to 0.967 whereas 0.945 for the second set, respectively. Same utilizing the RMS regression method, the constants for the Eq. (3) fatigue life estimation model have been estimated along with the correlation factor, equal to 0.972. The model constants for the above-mentioned three equations are summarized in Table 5 whereas the regression curve, along with the experiment points for unnotched and notched specimens, as well as for the U-Shape part, are reported in Fig. 15a, for the Eq. (2) models, and in Fig. 15b, for the Eq. (3) model, respectively.

As previously mentioned, the reasoning behind the separation of Eq. (2) into two sub-equations, relevant for LCF and HCF, is represented by the different influences that the stress triaxiality has at LCF and HCF. This fact has been observed, experimentally, by means of the SEM pictures analysis where, for the case of LCF, the polymer matrix presented a more clean fracture surface with almost no deformation of the polymer matrix, whereas, for HCF the fracture surface presented a more irregular shape with clear signs of a strong matrix deformation.

The two m_1 and m_2 constants have been calculated in order to maximize the correlation factor and it is interesting to notice how, for LCF, the m_1 constant is very close to the slope of the ΔK_{th} for long cracks for the linear elastic fracture mechanics, as presented in Atzori and Lazzarin [34].

On the other hand, the value of m_2 which maximizes the correlation factor is zero, a fact which shows the fainting importance of the stress triaxiality term $\sigma_H/\overline{\sigma}_{vM}$ of Eq. (2) for HCF. In addition to that, the comparison between the other two model constants (A_1,c_1 vs A_2, c_2) shows that the starting point ($N_f = 1$) for the LCF curve has a higher value for the strain function in comparison to the HCF, but a less negative exponent. In Fig. 15a, the curve relevant for static failure and LCF results to be higher than that of HCF and this effect is conditioned by the local strain concentration and absence of matrix deformation, especially for the case of the notched specimens. This fact makes the calculated values of the strain function to be higher for the former curve than the latter one. In order to avoid this discontinuity in the curve, the model Eq. (3) has been developed and the results, presented in Fig. 15b, are hereafter discussed.

As concerns the latter proposed fatigue life estimation model, Eq. (3), the effect of static failure, LCF and HCF have been all accounted for by means of a single equation. In addition to that, the high strain concentration arising in the case of static failure has been also scaled-down, allowing to obtain a single value-point for $N_f = 1$. In addition to that, the logarithmic part of Eq. (3) allows accounting for the reduction of the strain concentration effect for an increasing number of cycles to failure. The argument of the logarithmic function, $\varepsilon_{f,\,i}/\varepsilon_{\max,\,i}$, represented by the ratio between the total equivalent von Mises strain at failure (static) and the maximum value for the total equivalent von Mises strain for a cyclic loading condition, allows defining the position of the maximum point of the loading cycle, taking as a reference the static failure strain and acts as a sort of mean strain correction factor. The value $\varepsilon_{f,\,i}$ is not constant but it varies according to the considered geometry and has to be estimated by means of experiments or numerical simulations.

As shown in Fig. 15b, equation model (3) allows having a smooth transition between static failure, LCF and HCF. The starting point of the model, $N_f = 1 \rightarrow A = 0.5$, is determined by the first and second terms of the equation, whose role is to scale down the local strain concentration taking as reference the equivalent total von Mises strain, static failure, for the unnotched specimen $\varepsilon_{f,\,S\_UN}$. The results of both strain functions, Eqs. (2) and (3), for the unnotched and notched specimens, are reported in Table 6.

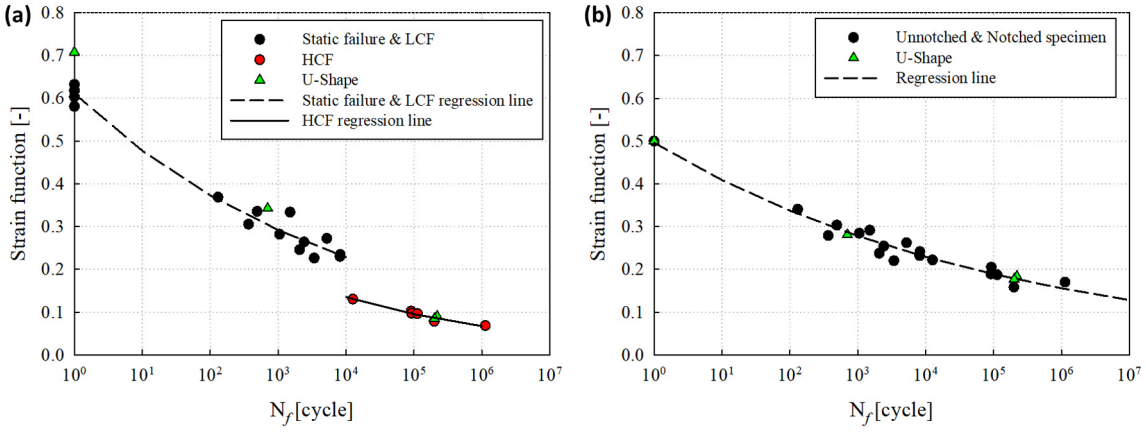

Fig. 15. Experimental points, including the U-Shape validation part, and regression curves for the (a) Eq. (2) model and (b) Eq. (3).

Table 6
Strain functions predictions for the equation models (2) and (3).

Loading condition	Case	Geometry	N_f	Eq. (2) model	Eq. (3) model
Static	EXP.2	Unnotched	1	0.581	0.500
	Case#1	#1	1	0.619	0.500
	Case#2	#2	1	0.617	0.500
	Case#3	#3	1	0.632	0.500
	Case#4	#4	1	0.603	0.500
Cyclic	#4N	#2	130	0.369	0.340
	#2N	#1	367	0.305	0.279
	#5N	#3	490	0.335	0.303
	#3U	Unnotched	1049	0.282	0.284
	#7N	#4	1500	0.333	0.291
	#7U	Unnotched	2066	0.246	0.237
	#3N	#2	2400	0.264	0.254
	#6U	Unnotched	3386	0.226	0.220
	#1N	#1	5214	0.272	0.262
	#2U	Unnotched	8140	0.230	0.232
	#1U	Unnotched	8217	0.234	0.241
	#6N	#3	12,630	0.130	0.222
	#8N	#4	91,220	0.102	0.189
	#8U	Unnotched	92,286	0.097	0.205
	#4U	Unnotched	112,497	0.096	0.187
	#5U	Unnotched	198,936	0.078	0.158
	#9U	Unnotched	1,127,661	0.068	0.170

The strain function values for the U-Shape part have been estimated by extrapolating the results of stresses and strains from the calculation steps of the ABAQUS numerical simulation relevant for the experimental minimum and maximum stroke amplitudes and inputting them into Eqs. (2) and (3). Afterward, the resulting non-linear equation with the unknown quantity N_f has been solved by means of the Newton-Raphson method and the results have been compared with the experimental ones, as summarized in Table 7. For the case of the Eq. (3) model, the static failure point of the U-Shape is automatically shifted to that of the static failure of the unnotched specimen, thanks to the combined effect of term one and two of Eq. (3). As shown in Table 7, both models have a good capability of estimating the cycles to failure also for the complex U-Shape geometry, not utilized in the regression calculation. However, although the Eq. (3) model is more complex and requires more input data, its accuracy is higher for both for LCF and HCF. In addition to that, the Eq. (3) model allows a softer transition between LCF and HCF, thus it shall be more accurate for the case of results those happen to be close to the boundary regions between Eqs. (2.1) and (2.2).

10. Conclusions

The research work presented in this paper has shown the possibility of estimating the fatigue life of components made of short fiber reinforced polymer on the basis of the local fiber length and orientation distributions. Both proposed fatigue models have shown their ability of properly predicting the fatigue life of the validation part, with reasonable accuracy. In addition to that, the results concerning the material characterization and SEM image analysis on the tested specimens fill a gap in the literature concerning the material characterization of injection molded components filled by short carbon fibers and the results of this paper might be of interest of other scholars dealing with this material. Finally, the utilized procedure for the mapping of the fiber length and orientation distributions for the precise estimation of the mechanical properties of injection-molded components has proven its reliability and should be therefore utilized if an accurate estimation of the mechanical performances of these typologies of parts is aimed to be achieved.

Table 7
Results comparison for the fatigue life prediction of the U-Shape part.

Model	N_f	FEM result	Model prediction	Variation [%]
Eq. (2)	1	0.707	0.611	13.7
	220,000	0.089	0.085	5.6
	700	0.342	0.303	11.2
	200,000	0.084	0.086	2.4
Eq. (3)	1	0.500	0.496	0.7
	220,000	0.184	0.177	3.6
	700	0.281	0.287	2.0
	200,000	0.176	0.178	1.3

CRediT authorship contribution statement

Luca Quagliato: Conceptualization, Formal analysis, Writing - original draft, Writing - review & editing. **Yonghee Kim:** Investigation, Data curation. **João Henrique Fonseca:** Software. **Dosuck Han:** Supervision. **Seungjong Yun:** Funding acquisition. **Hyungtak Lee:** Resources. **Nara Park:** Resources. **Hyungyil Lee:** Supervision. **Naksoo Kim:** Project administration.

Declaration of competing interest

The authors declare that they have no known competing financial interests or personal relationships that could have appeared to influence the work reported in this paper.

Acknowledgments

This work was supported by the Carbon Industrial Cluster Development Program (10083609) funded by the Ministry of Trade, Industry & Energy (MOTIE, Korea), by the Basic Science Research Program through the National Research Foundation of Korea (NRF) funded by the Ministry of Education (2019R1I1A1A01062323) and by the National Research Foundation of Korea (NRF) grant funded by the Korean government (MSIP: Ministry of Science, ICT and Future Planning) No. NRF-2018M2A8A4083765). These supports are gratefully acknowledged.

The research data related to this article are partially made available through the supplementary material and are all available on request to the corresponding author.

References

[1] Y. Wan, J. Takahashi, Tensile properties and aspect ratio simulation of transversely isotropic discontinuous carbon fiber reinforced thermoplastics, Compos. Sci. Technol. 137 (2016) 167–176.
[2] T. Ishikawa, K. Amaoka, Y. Masubuchi, T. Yamamoto, A. Yamanaka, M. Arai, J. Takahashi, Overview of automotive structural composites technology developments in Japan, Compos. Sci. Technol. 155 (2018) 221–246.
[3] H. Ning, S. Pillay, U.K. Vaidya, Design and development of thermoplastic composite roof door for mass transit bus, Mater. Des. 30 (2009) 983–991.
[4] A. Launay, M.H. Maitournam, Y. Marco, I. Raoult, Multiaxial fatigue models for short glass fiber reinforced polyamide – part I: nonlinear anisotropic constitutive behavior for cyclic response, Int. J. Fatigue 47 (2013) 382–389.
[5] A. Launay, M.H. Maitournam, Y. Marco, I. Raoult, Multiaxial fatigue models for short glass fibre reinforced polyamide. Part II: fatigue life estimation, Int. J. Fatigue 47 (2013) 390–406.
[6] C.S. Lee, H.J. Kim, A. Amanov, J.H. Choo, Y.K. Kim, I.S. Cho, Investigation on very high cycle fatigue of PA66-GF30 GFRP based on fiber orientation, Compos. Sci. Technol. 180 (2019) 94–100.
[7] A. Bernasconi, P. Davoli, A. Basile, A. Filippi, Effect of fibre orientation on the fatigue behaviour of a short glass fibre reinforced polyamide-6, Int. J. Fatigue 29 (2007) 199–208.
[8] M. Kawai, H. Takeuchi, I. Taketa, A. Tsuchiya, Effects of temperature and stress ratio on fatigue life of injection molded short carbon fiber-reinforced polyamide composite, Compos. Part A 98 (2017) 9–24.
[9] N.G. Karsli, A. Aytac, Tensile and thermomechanical properties of short carbon fiber reinforced polyamide 6 composites, Compos. Part B 51 (2013) 270–275.
[10] S.Y. Fu, B. Lauke, Effects of fiber length and fiber orientation distributions on the tensile strength of short-fiber-reinforced polymers, Compos. Sci. Technol. 56 (1996) 1179–1190.
[11] C. Capela, S.E. Oliveira, J. Pestana, J.A.M. Ferreira, Effect of fibre length on the mechanical properties of high dosage carbon reinforced, Procedia Struct. Integr. 5 (2017) 539–546.
[12] F. Rezaei, R. Yunus, N.A. Ibrahim, Effect of fiber length on thermomechanical properties of short carbon fiber reinforced polypropylene composites, Mater. Des. 30 (2009) 260–263.

[13] H. Mehdipour, P.P. Camanho, G. Belingardi, Elasto-plastic constitutive equations for short fiber reinforced polymers, Compos. Part B 165 (2019) 199–214.
[14] A. Launay, M.H. Maitournam, Y. Marco, I. Raoult, F. Szmytka, Cyclic behaviour of short glass fibre reinforced polyamide: experimental study and constitutive equations, Int. J. Plast. 27 (2011) 1267–1293.
[15] M.F. Arif, N. Saintier, F. Meraghni, J. Fitoussi, Y. Chemisky, G. Robert, Multiscale fatigue damage characterization in short glass fiber reinforced polyamide-66, Compos. Part B 61 (2014) 55–65.
[16] A. Launay, Y. Marco, M.H. Maitournam, I. Raoult, F. Szmytka, Cyclic behavior of short glass fiber reinforced polyamide for fatigue life prediction of automotive components, Procedia Eng. 2 (2010) 901–910.
[17] H.C. Tseng, Y.J. Chang, T.C. Wang, C.H. Hsu, R.Y. Chang, Three Dimensional Predictions of Fiber Orientation for Injection Molding of Long Fiber Reinforced Thermoplastics, SPE ACCE Conference, 2013.
[18] A.N. Oumer, O. Mamat, A study of fiber orientation in short fiber-reinforced composites with simultaneous mold filling and phase change effects, Compos. Part B 43 (2012) 1087–1094.
[19] J.H. Phelps, C.L. Tucker III, An anisotropic rotary diffusion model for fiber orientation in short- and long-fiber thermoplastics, J. Non-Newtonian Fluid Mech. 156 (2009) 165–176.
[20] Autodesk Moldflow Plastic Insight Manual, http://help.autodesk.com/view/MFIA/2019/ENU/.
[21] J.H. Phelps, Processing-microstructure models for short-and long-fiber thermoplastic composites, Diss. Abstr. Int. Section B 70–06 (2009) 3752–3950.
[22] S. Mortazavian, A. Fatemi, Fatigue behavior and modeling of short fiber reinforced polymer composites: a literature review, Int. J. Fatigue 70 (2015) 297–321.
[23] E. Belmonte, M. De Monte, C.J. Hoffmann, M. Quaresimin, Damage initiation and evolution in short fiber reinforced polyamide under fatigue loading: influence of fiber volume fraction, Compos. Part B 113 (2017) 331–341.
[24] M. Kamal, M.M. Rahman, M.S.M. Sani, Application of multibody simulation for fatigue life estimation, Int. J.Automot.Mech. Eng. 7 (2013) 912–923.
[25] W.D. Pilkey, Peterson's Stress Concentration Factors, 2nd ed John Wiley & Sons, Inc, 1997.
[26] J. Hartmann, E. Moosbrugger, A. Büter, Variable amplitude loading with components made of short fiber reinforced polyamide 6.6, Procedia Eng. 10 (2011) 2009–2015.
[27] P. Raposo, J.A.F.O. Correia, A.M.P. De Jusus, R.A.B. Calcada, G. Lesiuk, M. Hebdon, A. Fernández-Canteli, Probabilistic fatigue S-N curves derivation for notched components, Frattura ed Integrità Strutturale (42) (2017) 105–118.
[28] A. Bernasconi, E. Conrado, P. Hine, An experimental investigation of the combined influence of notch size and fibre orientation on the fatigue strength of a short glass fibre reinforced polyamide 6, Polym. Test. 47 (2015) 12–21.
[29] B.R.K. Blackman, H. Steininger, J.G. Wiliams, K. Zuo, The fatigue behaviour of ZnO nano-particle modified thermoplastics, Compos. Sci. Technol. 122 (2016) 10–17.
[30] J.H. Fonseca, G. Han, L. Quagliato, Y. Kim, J. Choi, T. Keum, S. Kim, D.S. Han, N. Kim, H. Lee, Design and numerical evaluation of recycled-carbon-fiber-reinforced polymer/metal hybrid engine cradle concepts, Int. J. Mech. Sci. 163 (2019), 105115.
[31] KOPA® KN111 PA6 Datasheet (Kolon Plastic), 2017.
[32] Torayca® T700S Datasheet (Toray Carbon Fibers America, Inc.), 2016.
[33] Autodesk advanced material exchange manual, knowledge.autodesk.com/support/helius-pfa.
[34] B. Atzori, P. Lazzarin, A three-dimensional graphical aid to analyze fatigue crack nucleation and propagation phases under fatigue limit conditions, Int. J. Fract. 118 (2002) 271–284.